Distortion prediction and geometry compensation using modified inherent strain method for additively manufactured Ti-6Al-4V

Refak Makeen [a], Kartikey Joshi [b], Mark H. Jhon [b], Patcharapit Promoppatum [a c]

[a]

Center for Lightweight Materials, Design, and Manufacturing, Department of Mechanical Engineering, Faculty of Engineering, King Mongkut's University of Technology Thonburi (KMUTT), Bangmod, Bangkok 10140, Thailand

[b]

Institute of High Performance Computing, A*STAR, 1 Fusionopolis Way, #16-16 Connexis, Singapore 138632, Singapore

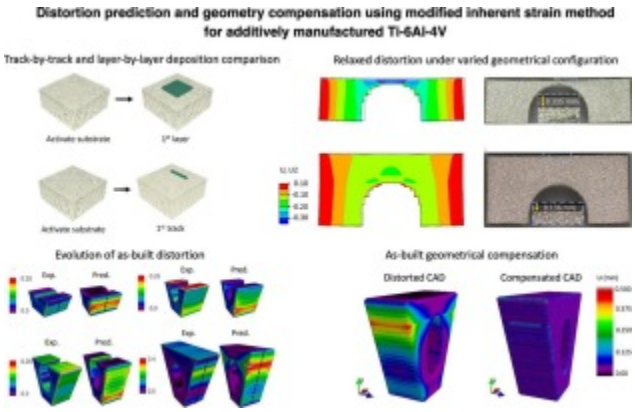
[c]

OsseoLabs Co. Ltd., Bangkok 10400, Thailand

Abstract

A laser powder bed fusion (LPBF) process enables the production of intricate geometries for specialized applications demanding high precision in various industries such as medical, aerospace, and automotive. However, substantial thermal gradients in the LPBF process often led to residual stress, resulting in noticeable distortion and potential part failure of fabricated parts. Therefore, the present work investigates distortion prediction and geometry compensation for additively manufactured Ti-6Al-4V components employing a modified inherent strain method. Unlike previous studies, both relaxed distortions from substrate removal and as-built distortion are considered, incorporating specimens with varying geometrical features such as height and thickness. The study aims to comprehensively evaluate the efficacy of the modified inherent strain approach in capturing distortion under different build scenarios and assess the effectiveness of geometrical compensation in minimizing as-built distortion. Overall, we found that numerical models effectively capture relaxed deflection for samples with varied geometrical features, showing reasonable agreement with experimental results. Additionally, the as-built distortion of samples with thicknesses of 5 mm and above is well-predicted, with an average deviation between numerical and experimental results of approximately 0.125 mm. Nonetheless, we noted the challenge in capturing out-of-plane distortion for thin wedges, suggesting avenues for future investigation. Furthermore, geometry compensation reduces maximum distortion from 0.68 to 0.28 mm and average distortion from 0.15 to 0.05 mm. Multiple iterations of compensation yield insignificant differences in distortion reduction, which suggests sufficient distortion alleviation from single compensation for geometries explored in the present work. Overall, the study provides valuable insights into distortion prediction and compensation strategies for additively manufactured Ti-6Al-4V components.

Graphical abstract



Keywords
Laser powder bed fusion process
Ti-6Al-4V
Modified inherent strain method
Residual stress
Distortion prediction
Geometry compensation

1. Introduction

Laser powder bed fusion (LPBF) uses computer-aided design (CAD) models to create 3D geometries layer-by-layer on a substrate. This technology can manufacture complex, customizable shapes that are difficult to produce with conventional methods [[1], [2], [3]]. LPBF is primarily used in the biomedical, automotive, and aerospace industries, where highly intricate components are essential [4]. Due to repeated melting and cooling cycles during fabrication, residual stresses in parts fabricated by LPBF are mostly inevitable. Mercelis and Kruth [5] explain the origin of residual stress with two phenomena, namely the temperature gradient mechanism and the cool-down phase mechanism. The temperature gradient mechanism describes the compression in the heated region due to inhibited expansion from the surrounding cooler area. The cool-down phase mechanism describes the tensile stress at the top during the cooling of the heated region. Excessive residual stress can negatively affect LPBF parts, leading to sub-optimal mechanical properties [6], geometrical distortion [7,8], and part failure from cracking [4,9].

Various experimental approaches have been studied to alleviate residual stresses in LPBF parts. Researchers have examined the influence of manufacturing parameters, finding that optimizing laser power, scan length, scan velocity, and scanning pattern can reduce overall residual stresses [[10], [11], [12]]. Additionally, post-treatment processes, particularly annealing, have been shown to relax residual stresses in LPBF fabrications [11,[13], [14], [15]]. Chen et al. [16] explored in-situ stress control by managing thermal accumulation during the process, achieving stress reduction comparable to post-treatment methods. Moreover, residual stresses and distortions can be modeled using fully coupled thermomechanical simulations that incorporated heat source models, laser scanning strategies, and other process parameters [17,18]. Although the implementation of a fully coupled thermomechanical model can be straightforward, the method is often computationally demanding, limiting predictions to one or a few layers. Thus, in addition to fully coupled thermomechanical models, the modified inherent strain method has been widely adopted for efficient residual stress prediction at the part-scale level. The method was initially developed for welding problems, as shown by Murakawa et al. and Wang et al. [19,20]. However, the modified

inherent strain method has since been extended to the prediction of the LPBF process. The modified inherent strain method begins by performing a meso-scale thermomechanical simulation, which considers relevant process conditions and temperature- as well as rate-dependent material properties, to predict stress formation in a single layer. Subsequently, the inherent strains are extracted from meso-scale results and mapped onto activated layers for part-scale calculation. With the modified inherent strain method, only the static mechanical solver is employed, and the activated layer is assumed to generate predetermined stress profiles from the meso-scale calculation. Several studies have explored and assessed the fidelity of the modified inherent strain method for part-scale prediction of the LPBF process [21].

Promoppatum and Uthaisangsuk [22] implemented the modified inherent strain method for additively manufactured Inconel 718. The residual stress profiles were collected at different build stages. They compared the predicted stress at the part level with neutron diffraction-based residual stress measurements from Bayerlein et al. [23]. Both the prediction and experimental results showed great agreement. Bayraktar and Demir [24] demonstrated that the modified inherent strain method could reduce the calculation time by six times, and a similar study by Patil et al. [25] mentioned that a layer agglomeration method can achieve the computational time reduction by 10–25 times compared to a fully coupled thermomechanical model. Abarca et al. [26] studied residual stress in thin-walled structures at both micro and macro scales. They used coupled thermomechanical simulation and the inherent strain method for macro-scale simulations. The inherent strain method reduced computational time from 130 to 1.5 h compared to the fully coupled model. To date, the modified inherent strain methods have been acknowledged in the previous works for their capability in predicting reasonably accurate residual stress as seen Promoppatum and Uthaisangsuk [22], Promoppatum and Yao [12], and Chen et al. [27].

In addition to stress prediction, the modified inherent strain method has been utilized in several studies for distortion prediction. For instance, Chen et al. [28] employed this method to accurately predict distortion in a double cantilever beam and a canonical part fabricated using LPBF. Similarly, Liang et al. [29] used the modified inherent strain method to predict distortion in parts made using the direct energy deposition AM technique. Once distortion is predicted, previous studies attempt to reduce as-built distortion by modifying the CAD model to compensate for the anticipated distortion. Afazov et al. [30] utilized the inherent strain method to model the distortion of a thin manifold structure, followed by compensation by adjusting original CAD files. They compared the results with experimental distortion obtained using an optical 3D scanner. The results showed a reduction in distortion from approximately ±400 µm to ±100 µm. A similar study by the same author [31] involved distortion prediction through thermomechanical analysis, followed by geometric compensation conducted in two steps: finite element analysis (FEA) to invert the original geometry and interpolation of optical scan results from experiments to invert the nominal geometry. The distortion was reduced from a range of ±200 µm in the non-compensated part to about ±45 µm after conducting the FEA-based compensation, and the optical scanning-based compensation showed distortion ranging between −15 µm and 70 µm. Performing distortion compensation using a numerical model has several benefits. Firstly, while one may scan the printed model and correct it based on measured distortions, performing such a task requires significant resources, making purely experimental compensation less practical. Secondly, numerical simulation allows exploration of different strategies; for example, one can assess efficiently the effects of geometrical variation, part orientation, and compensation iteration.

Although previous works have shown initial success for the modified inherent strain method, many questions remain. Firstly, most previous studies employed a single geometry in their investigations. Abarca et al. [26] applied the inherent strain method to a semi-circular thin-walled part, comparing residual distortion with other modeling methods. Setien et al. [32] predicted distortion in a twin cantilever beam. Similarly, many studies, such as those by Promoppatum and Uthaisangsuk [22], Chen et al. [28], and Liang et al. [29], used cantilever beams and block structures. From previous works, it could be noticed that an assessment of the modified inherent strain method to capture relaxed and as-built distortion for geometries with varied features has been lacking. Thus, the question arises whether the modified inherent strain method can accurately capture residual stress formation under varied geometric attributes. Secondly, although previous works using the modified inherent strain method simplified the scan patterns by utilizing the layer-by-layer activation, one can implement the part-scale build using the track-by-track activation, which presents more realistic deposition patterns as previously pointed out by Liang et al. [29]. However, the trade-off between resource consumption and numerical accuracy between layer-by-layer and track-by-track activations has been rarely discussed in previous works. Thirdly, the geometrical compensation used in previous works does not consider multiple iterations. For example, Afazov et al. performed only a single geometrical compensation based on the predicted distortion of the CAD model [31,33]. Thus, although the use of multiple iterations has been introduced in commercial software such as Simcenter 3D software [34], the effectiveness of distortion alleviation from multiple geometrical compensations is largely unexplored.

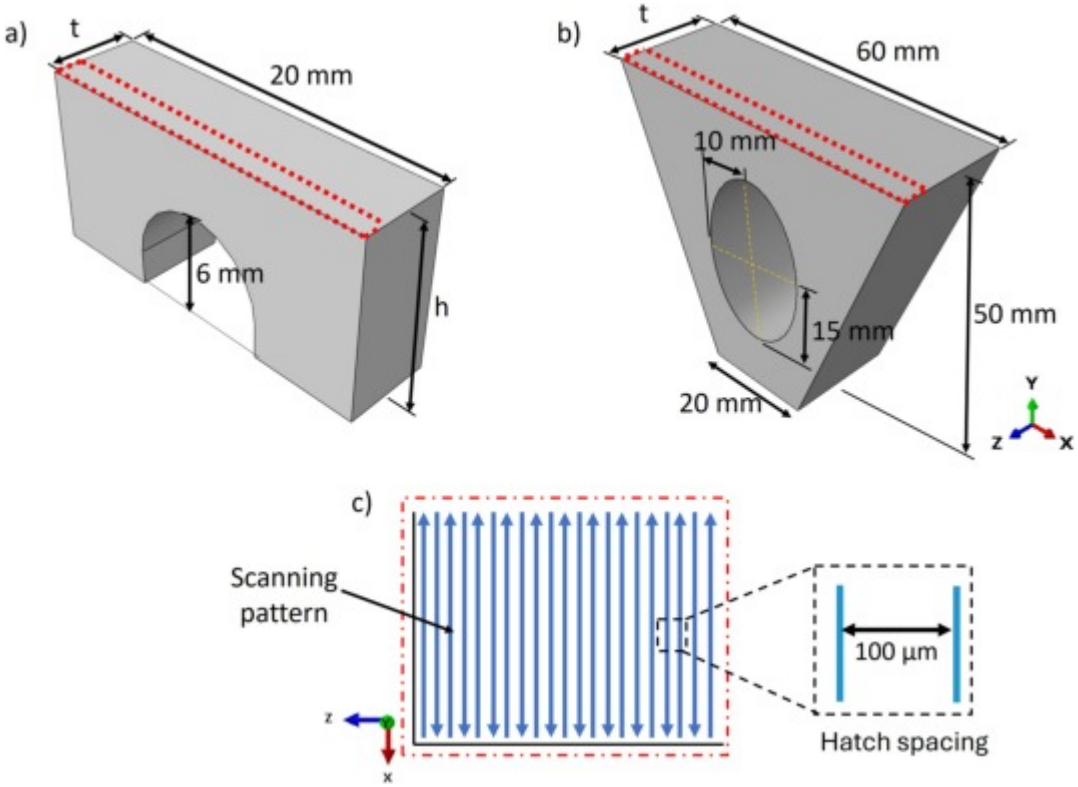
Therefore, the present work aims to comprehensively assess the effectiveness of the modified inherent strain approach in predicting distortion in additively manufactured specimens. Both experimental and numerical methods will be employed and compared. The study will involve building bridge-like structures with varying heights and thicknesses to determine the method's ability to capture geometry-dependent responses. Additionally, wedge structures with varying thicknesses will be used to explore as-built distortion. This work will also evaluate the effects of different deposition sequences on computational time and distortion, comparing layer-by-layer and track-by-track methods. Lastly, the effectiveness of CAD compensation in reducing as-built distortion will be assessed through comprehensive comparisons of numerical and experimental results, including full 3D scans and multiple compensation strategies.

2. Experiments

2.1. Specimen design

In the present work, we explored two test cases: the deflection after substrate removal and the as-built distortion. The former case allowed us to assess the capability of the numerical framework in predicting the distortion of additively manufactured specimens with different geometrical features. The latter case was used to implement the CAD correction method based on predicted distortion. To assess the part deflection after substrate removal, we adopted the bridge curvature method (BCM), as shown by Kruth et al. [35]. The deflection of the bridge after relaxation can be used to assess the magnitude of residual stress, as demonstrated previously by Promoppatum and Yao [12], Le Roux et al. [36], and Ma et al. [37]. Such structures have been used to study the effect of scan hatch patterns, laser parameters, and material properties on resulting residual stress. However, rather than exploring the effect of process parameters, our interest lies in assessing the resulting deflection under changing geometrical features. As a result, the bridge was constructed with varied heights (h) and thicknesses (t), as shown in Fig. 1a. Four different heights of 6.5, 7, 8, and 10 mm, as well as three different

thicknesses of 1, 3, and 10 mm, were chosen, resulting in twelve different bridge specimens. For the as-built distortion, we adopted wedge specimens with elliptical holes, as shown in Fig. 1b. According to Lestandi et al. [38], these specimens reveal complex stress profiles, allowing us to examine the effectiveness of the distortion prediction and CAD compensation framework. Additionally, four thicknesses of 1, 5, 10, and 20 mm were chosen for the wedge samples. In addition, Fig. 1c displays the scan pattern used in the present work. We adopted a zigzag scan pattern with a hatch spacing of 100 µm between each hatch line. There is no rotation of hatch patterns between each deposition layer.



1. Download: Download high-res image (222KB)
2. Download: Download full-size image

Fig. 1. a) Bridge specimen design with varied heights and thicknesses for capturing deflection after the substrate removal and b) Wedge with the elliptical hole with varied thicknesses for examining the as-built distortion, c) Zigzag scan pattern with a hatch spacing of 100 µm.

2.2. Sample fabrication

Specimens were made using the TRUMPF TruPrint 1000, a laser powder bed fusion (LPBF) system, with Ti-6Al-4V. The Ti-6Al-4V powders were supplied by AP&C GE Additive, with particle sizes varying between 30 and 45 µm. The SEM morphology and chemical composition of the powders can be found in our previous work [39]. All specimens were built using identical process parameters, as shown in Table 1. These process parameters were proven to provide fully dense parts. Additionally, the build substrate is also Ti-6Al-4V, where the specimens are placed directly on the substrate without any use of support structures.

Table 1. LPBF process parameters for Ti-6Al-4V specimens.

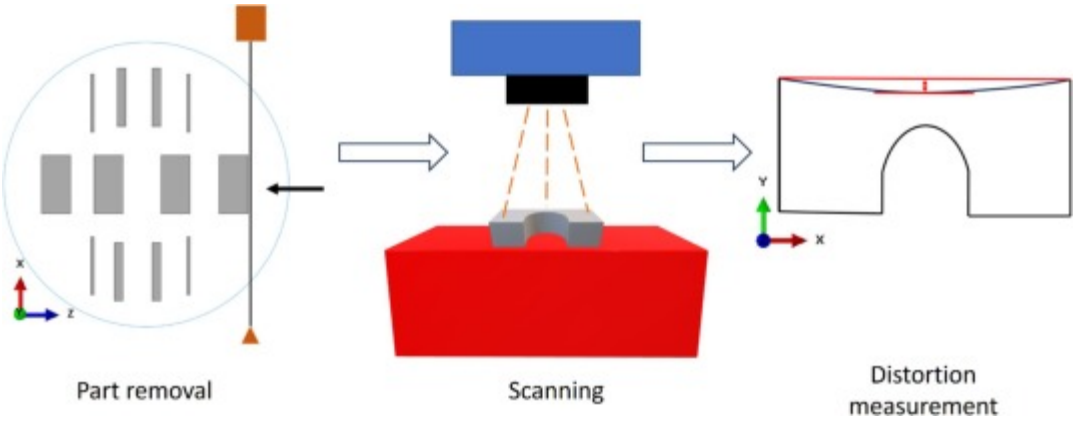
Process parameters	**Values**
Laser power	100 W
Scanning speed	1000 mm/s

Process parameters	Values
Layer thickness	30 μm
Laser diameter	50 μm
Hatch spacing	100 μm
Hatch pattern	Stripes

During fabrication, the oxygen concentration was maintained below 100 ppm for all experiments in this study. Such build condition was typically used for LPBF of titanium as seen in previous works of Williams et al. [40] and Issariyapat et al. [41]. The oxygen control was achieved through a continuous and controlled supply of argon gas to the build chamber. The oxygen content was monitored by oxygen sensor in the build chamber throughout the print process. After printing, the samples were removed from the build chamber. Although we used a vacuum cleaner to eliminate loose powders, no other post-processing methods were performed on the specimens. For the bridge specimens, the build process took around 3 h, while the process took around 10 h for the wedge specimens.

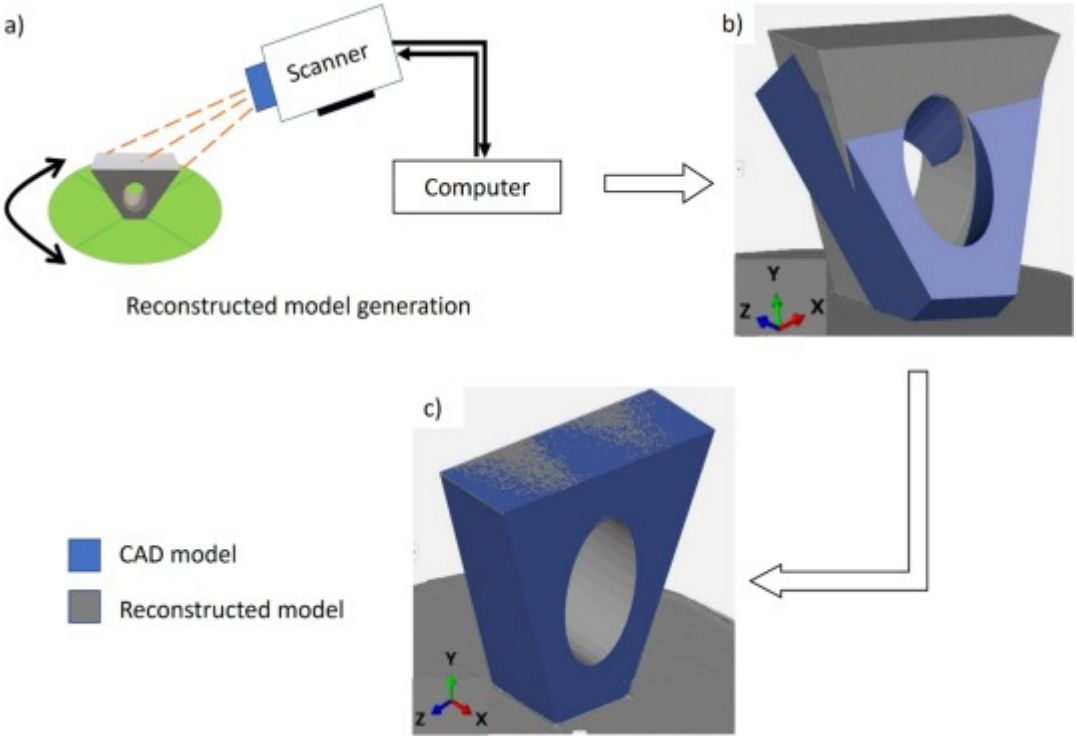
2.3. Relaxed and as-built distortion assessment

Fig. 2 illustrates the method required for distortion assessment of the relaxed specimens. Firstly, the printed samples were removed from the substrate using a wire electrical discharge machine. According to Fig. 2, the wire was aligned and cut along the short edge of the samples. The cutting alignment ensured that both legs of the bridge were removed simultaneously. Subsequently, high-resolution images of the detached specimens were acquired using a digital microscope, the Keyence VR 5000 series. Based on the acquired images, the deflection magnitude at the middle of the specimen was recorded. For each sample, two measurements were performed on each side of the specimen. In total, there were four measurements for each condition. The average and variance of deflection were subsequently calculated for further comparison with numerical simulations. Additionally, for as-built distortion assessment, the printed wedge underwent 3D scanning using an industrial 3D scanner, the ATOS Core 200. The scanning device captured 3D data by identifying reference points on the samples positioned on a rotatable platform. The 3D scanner has a coverage area of 200 × 150 mm^2 with a scanning tolerance of 0.08 mm. Prior to scanning, the scanner was calibrated by placing reference markers on both the positioning table and the part. These markers were recognized by the scanner as reference points [42]. During the scanning process, a high-resolution point cloud describing the object surfaces was obtained. Later, the point cloud could be reconstructed into a surface mesh representing the printed specimens. The comparison between the CAD and reconstructed model revealed the geometric deviation of the printed specimen from the CAD model. Fig. 3 summarizes the assessment procedure for as-built distortion.



1. Download: Download high-res image (85KB)
2. Download: Download full-size image

Fig. 2. Distortion assessment for sample's deflection because of stress relaxation from substrate removal.



1. Download: Download high-res image (149KB)
2. Download: Download full-size image

Fig. 3. Distortion assessment for as-built distortion from 3D scan and pre-alignment of CAD with reconstructed 3D models.

3. Numerical methodology

3.1. Modified inherent strain method

Residual stress in the LPBF process originates from repeated thermal cycles during laser scanning. A localized heat spot leads to rapid solidification and thermal contraction. Although thermomechanical simulations could be implemented to examine residual stress formation, as seen in Vastola et al. [43], Bian et al. [44], and Xiao et al. [45], extensive computational requirements are one of the primary challenges, prohibiting the extension of part-scale simulations. To resolve this challenge, residual stress simulation at a part level is often carried out using a modified inherent strain method. The

modified inherent strain method involves two steps: extracting and applying inherent strains [46]. To extract the inherent strain, a full thermomechanical simulation needs to be performed by incorporating detailed process parameters such as laser power, scan speed, layer thickness, and hatch patterns. Temperature-dependent material properties and the effect of liquid-solid phase changing must also be considered. The numerical results from a full thermomechanical model would provide resulting residual stress within the deposited layer, in which the stress components would be used to determine inherent strains [22]. The effect of process conditions on cooling rates and stress formation within a layer would be accounted in the full thermomechanical simulation, which is referred to as the meso-scale model. Subsequently, the inherent strains are applied to the modified inherent strain model by considering solely static mechanical analysis. The laser scanning pattern is lumped into the layer-by-layer deposition through element activation techniques, as previously seen in Setien et al. [32] and Singh et al. [47]. The model at this level is referred to as the macro-scale model. In the macro-scale model, since only a static solver is utilized, it could only show the resulting stress at the end of layer deposition. In the present work, the meso-scale residual stress was obtained from Promoppatum and Yao [12], who assessed stress formation under varied energy inputs and scan lengths. The choice of process conditions for numerical simulation was chosen according to experimental conditions shown in Table 1.

Based on the process conditions shown in Table 1, the energy flux is 2 J/mm^2, and the track scanning time is 20 ms. According to Promoppatum and Yao [12], these process conditions resulted in σ_{xx}, σ_{yy}, and σ_{zz} values of 800, 0, and 450 MPa, respectively. These stresses are the average values from the meso-scale model, where σ_{xx} and σ_{zz} represent the in-plane stress components parallel and perpendicular to the laser scanning direction, respectively, while σ_{yy} represents the out-of-plane stress component. The reason σ_{yy} is presumed to be zero is that when residual stress forms at the layer level, although the in-plane deformation is constrained by the surrounding materials, the out-of-plane deformation could occur without mechanical restraint. Therefore, σ_{yy}, which represents the out-of-plane stress, is close to zero.

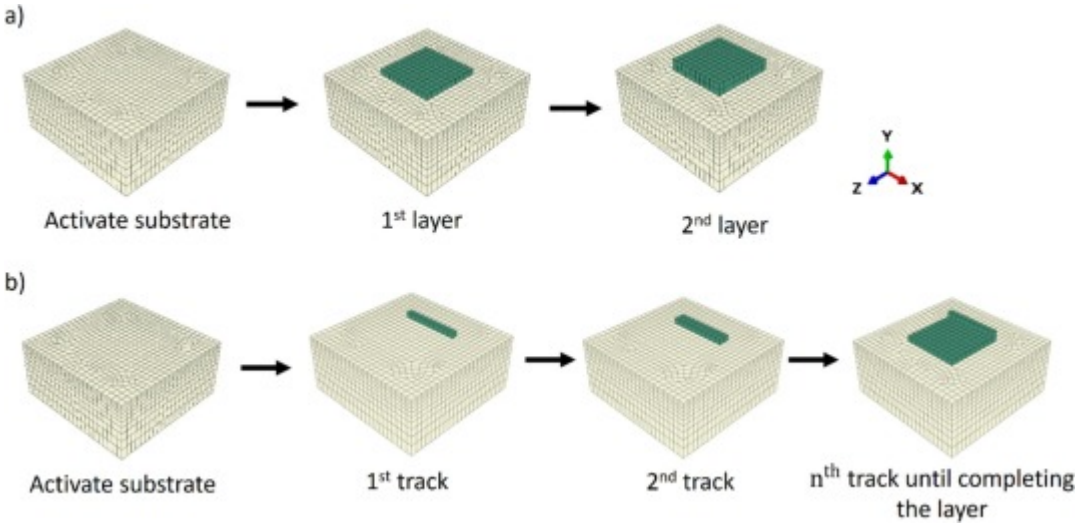
In addition, the elastic modulus (E), Poisson's ratio (ν), and initial yield stress (σ_{y0}) are 110 GPa, 0.3, and 1015 MPa, respectively [12,48]. Subsequently, the modified inherent strain method is implemented in Abaqus/Standard. The inherent strains ($\varepsilon*$) were used to update the part-scale residual stresses. A Fortran-based UMAT user subroutine together with the model change function were used to achieve layer-by-layer sequential simulation. The model change interaction assists the activation of a partitioned layer at each study step. Besides, the user subroutine was used to specify the pre-defined inherent strains for the activated layer. According to Eq. (1), the total strain (εtotal) consists of elastic (εel), plastic (εpl), and thermal (εth) strains. The inherent strain represents the inelastic strain, which is shown in Eq. (2), and the residual stress at the activated layer could be determined from Eq. (3). The UMAT would define inherent strains (ε^*) in the activated layer, which leads to the targeted stress as shown in Table 2. In addition to the activated layer, the solid element is specified with a von Mises yield criterion and Voce hardening model as described in Eq. (4). The material properties and residual stress input of the present work are summarized in Table 2, and they will be kept constant for all the test cases in the present study. Additionally, a voxel-based meshing was adopted in the present work. Based on the Abaqus naming convention, an eight-node brick element with reduced integration, C3D8R, was utilized. All simulations were performed with AMD Ryzen 95,950× processor of 32 cores and 128 GB RAM.(1)$\varepsilon\text{total}=\varepsilon\text{el}+\varepsilon\text{pl}+\varepsilon\text{th}(2)\varepsilon*=\varepsilon\text{total}-\varepsilon\text{el}(3)\sigma=D\varepsilon\text{el}(4)\sigma y=\sigma y0+H1-\exp-\beta\varepsilon\text{pl}$

Table 2. Material properties and residual stress inputs from Refs. [12,48].

Material properties	Values	Units
E	110	GPa
v	0.3	–
$\boldsymbol{\sigma}_{y0}$	1015	MPa
H	177	MPa
β	117	–
$\boldsymbol{\sigma}_{xx}$	800	MPa
$\boldsymbol{\sigma}_{yy}$	0	MPa
$\boldsymbol{\sigma}_{zz}$	450	MPa

3.2. Layer-by-layer and track-by-track deposition of residual stress simulation

As mentioned in the previous section, for the modified inherent strain method, the 3D model would be sliced into a series of macro layers, which are sequentially activated until the layer deposition is completed [21]. Fig. 4a shows an example of layer-based activation with two layers. However, layer activation may not capture the influence of path-dependent residual stress formation. For example, Wang et al. [49] and Ren et al. [50] developed numerical models to capture stress formation under various deposition patterns in the directed energy deposition process. The influence of different deposition sequences on stress formation is clearly shown in their works. Thus, we aim to evaluate the limitations of the layer-based modified inherent strain method by conducting an alternative approach based on track-by-track deposition, as seen in Fig. 4b. In the track-based method, once the 3D model is sliced into layers, each layer is further divided into deposition tracks. The actual deposition track should be based on the hatch spacing. However, to compromise computational costs, we relied on a lumped track, with a track size of 0.25 mm. In the track-based method, inherent strain is applied to the activated track, and the stresses of previously deposited tracks could respond accordingly. Although the track-based method would require much higher computational resources than the layer-based one, it is expected to more closely mimic the laser scanning pattern used for specimen fabrication.



1. Download: Download high-res image (285KB)
2. Download: Download full-size image

Fig. 4. a) Layer-by-layer deposition and b) Track-by-track deposition for layer-scale residual stress calculation.

3.3. CAD compensation based on predicted deformation

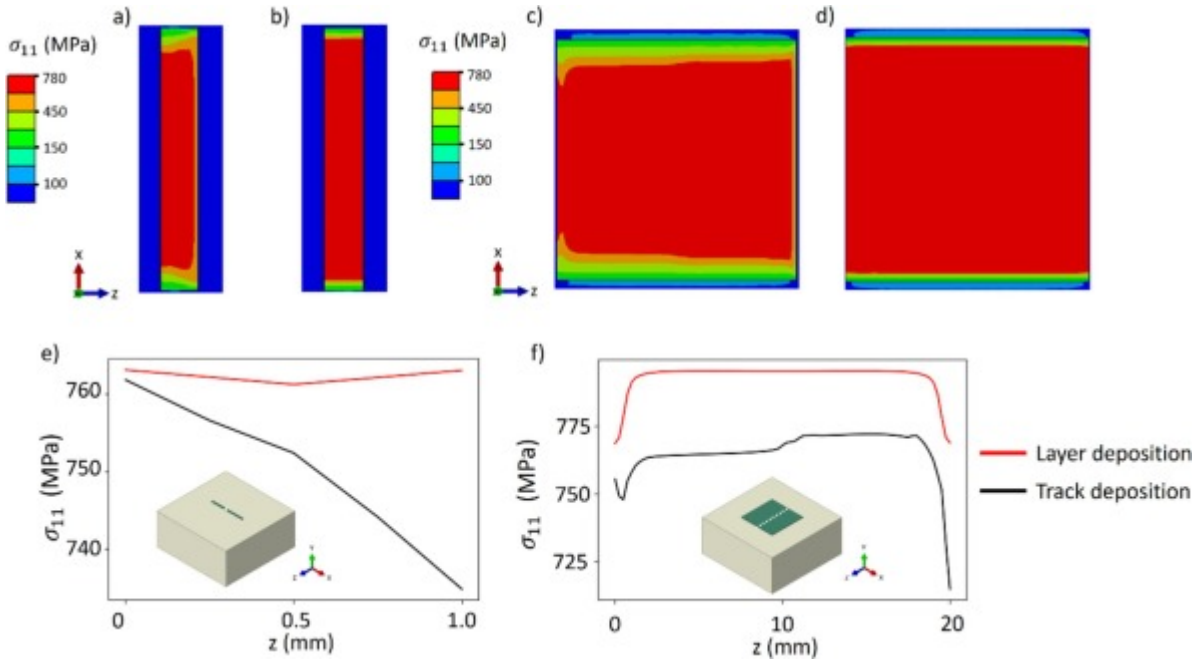
The compensation method used in the present work was similar to that of Afazov et al. [33]. This method involves predicting and compensating for part-scale distortion. The predicted distortion is negated and used to pre-distort the original CAD models. Subsequently, the pre-distorted models are re-simulated and printed to verify the compensation results. In addition, Eq. (5) describes the process of pre-distorting a 3D model. According to Eq. (5), the 3D model is converted into a point cloud, where x, y, and z represent the original coordinates of the geometry. Subsequently, u_{11}, u_{22}, and u_{33} represent the directional distortion in Cartesian coordinates for each point in the cloud. The directional distortion magnitudes were obtained from numerical predictions for the present work. Consequently, the original point clouds were modified according to the directional distortion, resulting in a compensated geometry in which the adjusted point clouds are denoted by x_i, y_i, and z_i.(5)Pxiyizipre−distorted=Px−u11iy−u22iz−u22inominal

4. Results and discussion

4.1. Mechanical comparison of track-by-track and layer-by-layer deposition method

Although the actual scan patterns in the AM process consist of multiple track depositions, the modified inherent strain method considers the lumped approach, where multiple track depositions are combined into a layer deposition. While the layer deposition in the modified inherent strain method has been proven to accurately capture experimental responses such as relaxed distortion and as-built stresses, the influence of track-by-track deposition on stress and distortion has not been extensively studied for specimens with different thicknesses.

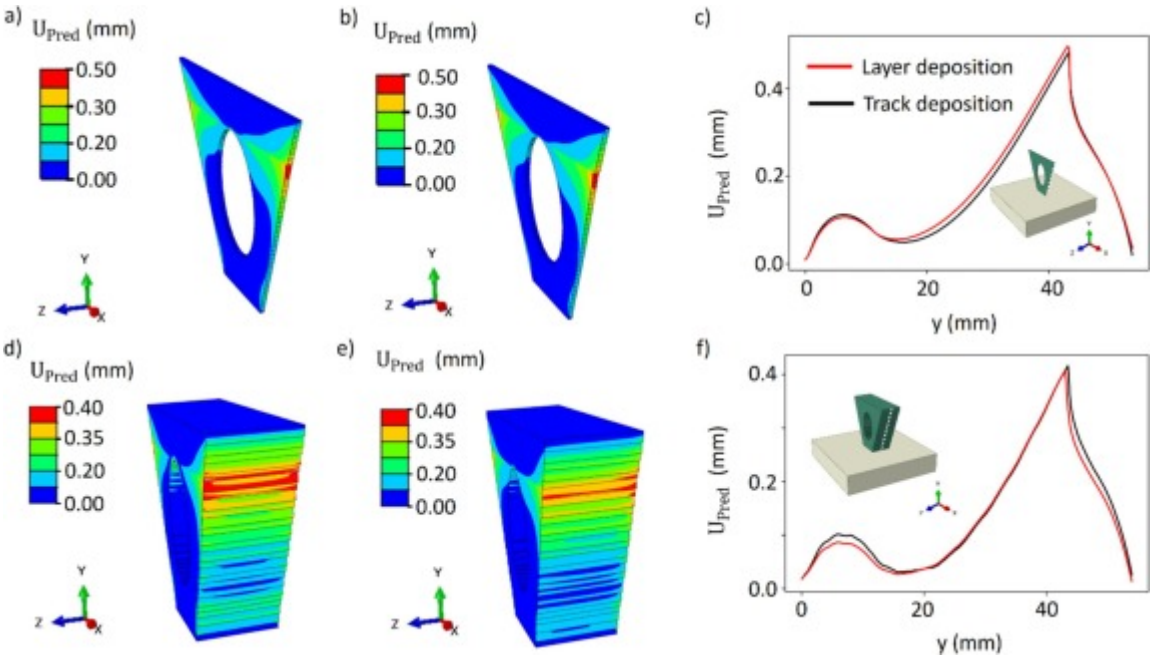
Fig. 5a to Fig. 5f compares the stress responses between track-by-track and layer-by-layer deposition of a single layer. We considered the single layer with a thickness of 1 and 20 mm, respectively. For the track-by-track deposition, the track size is 0.25 mm. As a result, four and eighty tracks were utilized for 1 and 20 mm thick specimens, respectively. Fig. 5a and Fig. 5b illustrate stress contours for two different depositions of a 1 mm thick specimen. Fig. 5a shows asymmetric stress contours at both ends for track-by-track deposition. However, more symmetric stress profiles are seen for layer deposition, as shown in Fig. 5b. We noticed that track-by-track deposition allows stress to alter from continuing deposition, in which such stress alteration is not seen with layer-by-layer deposition. A similar observation was seen for 20 mm thickness, as shown in Fig. 5c and Fig. 5d. Fig. 5c showed that track-by-track deposition led to non-uniform and relaxed resulting stresses within the layer. Fig. 5e and Fig. 5f reveal higher stress with layer-by-layer deposition. Track-by-track methods led to stress relaxation, which is more evident in a thicker layer. For example, at the end of the deposition, Fig. 5e showed that stress reduced from 763 to 734 MPa, approximately a 4 % reduction for a 1 mm thick sample. Nonetheless, stress reduction increased to approximately 7 % for a 20 mm thick sample, as shown in Fig. 5f. Overall, while we observed the effect of material deposition patterns, their effect on resulting stress is relatively small.



1. Download: Download high-res image (178KB)
2. Download: Download full-size image

Fig. 5. Stress contour at the first layer of 1 mm thickness specimen with a) track-by-track deposition and b) layer-by-layer deposition and for 20 mm thickness specimen with c) track-by-track deposition and d) layer-by-layer deposition, e) stress profiles of 1 mm thickness specimen with track-by-track and layer-by-layer depositions, and f) stress profiles of 20 mm thickness specimen with track-by-track and layer-by-layer depositions.

Subsequently, we carried out part-scale simulations of the wedges. Two thicknesses of 1 and 20 mm were chosen. Two deposition patterns, track-by-track and layer-by-layer methods, were compared. With layer deposition, the simulation took 14 and 37 h for the wedges with 1 and 20 mm thickness. However, with track deposition, the computational time escalated to 56 and 1650 h, respectively. Evidently, implementing track-by-track deposition led to a significant increase in required resources. Fig. 6a to Fig. 6f examine the predicted distortion of 1 and 20 mm wedges. Predicted distortion contours are shown in Fig. 6a and Fig. 6b, and Fig. 6c and Fig. 6d for 1 and 20 mm wedges, respectively. Overall, the distortion contours were largely similar for both deposition patterns, with the maximum distortion observed in the region around the ellipsoidal holes. Fig. 6e and Fig. 6f show the distortion profiles at the inclined surfaces. Based on two different deposition patterns, the average difference in predicted distortion was 0.0079 and 0.0071 mm for 1 and 20 mm wedges, respectively. Although the influence of deposition patterns is more noticeable in thicker samples, their effect is relatively small for the conditions explored in the present work.

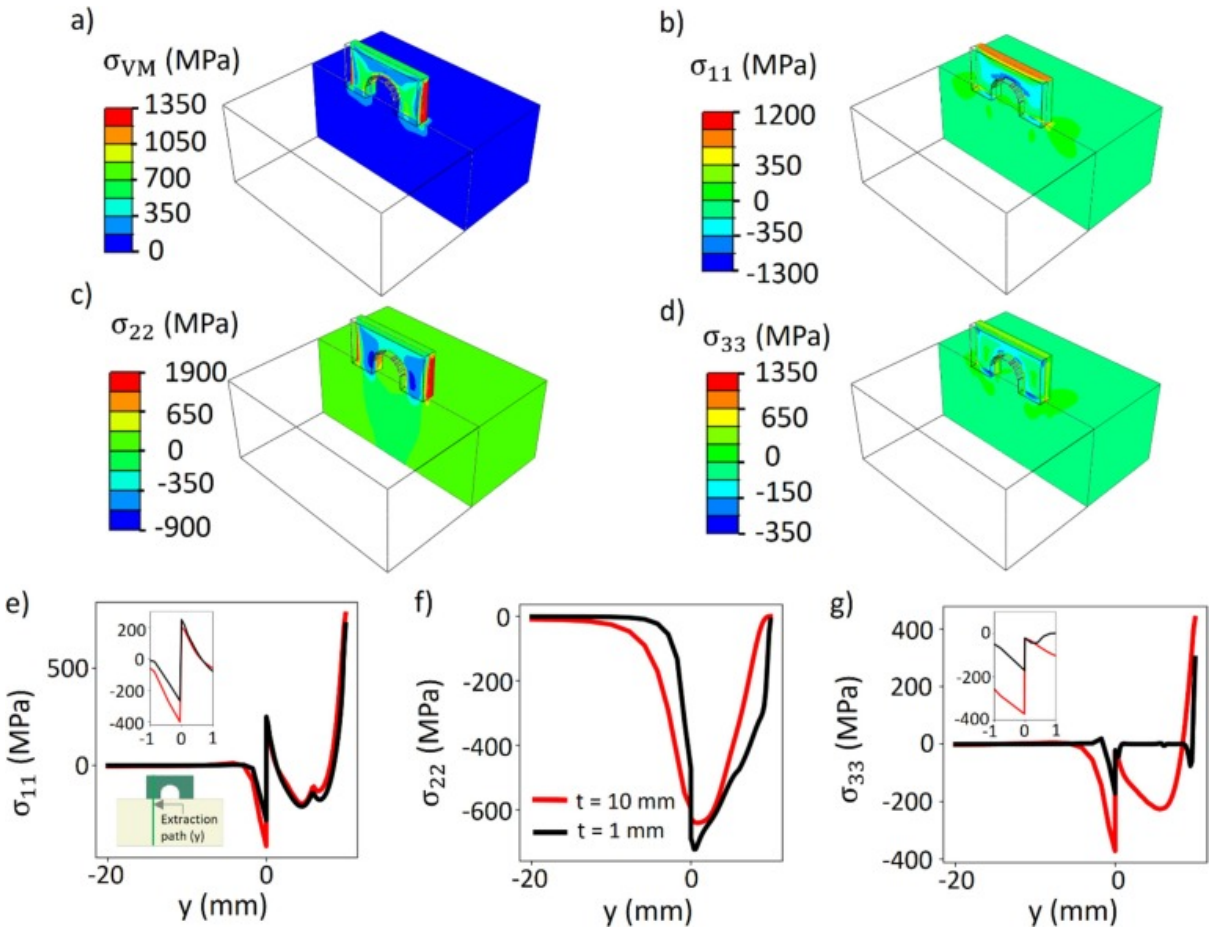


1. Download: Download high-res image (269KB)
2. Download: Download full-size image

Fig. 6. Predicted as-built distortion for the wedge with 1 mm thickness from layer-by-layer and track-by-track methods for (a-b) wedge with 1 mm thickness and (c-d) wedge with 20 mm thickness, and (e-f) distortion profiles along the inclined surface of the wedge from two different depositions for wedges with 1 and 20 mm thickness, respectively.

4.2. Stress distribution and relaxed distortion of bridge specimens

Based on the finding from the previous section, we considered only the layer-by-layer deposition for subsequent simulation results. Fig. 7a to Fig. 7d illustrate the stress contours of the bridge specimen with a height and thickness of 10 and 3 mm, respectively. The stresses are shown for σ_{mises}, σ_{11}, σ_{22}, and σ_{33}. According to Fig. 7b and Fig. 7d, large tensile stresses were observed at the top surface of the bridge sample. However, compressive stresses for σ_{11} and σ_{33} were seen shifting towards the middle section of the specimens. Additionally, according to Fig. 7b, although σ_{22} is mostly negligible at the top surface, a large compression of σ_{22} is seen at the interior region of the sample. These stress contours align well with previous experimental and numerical studies [22,28,29,35].



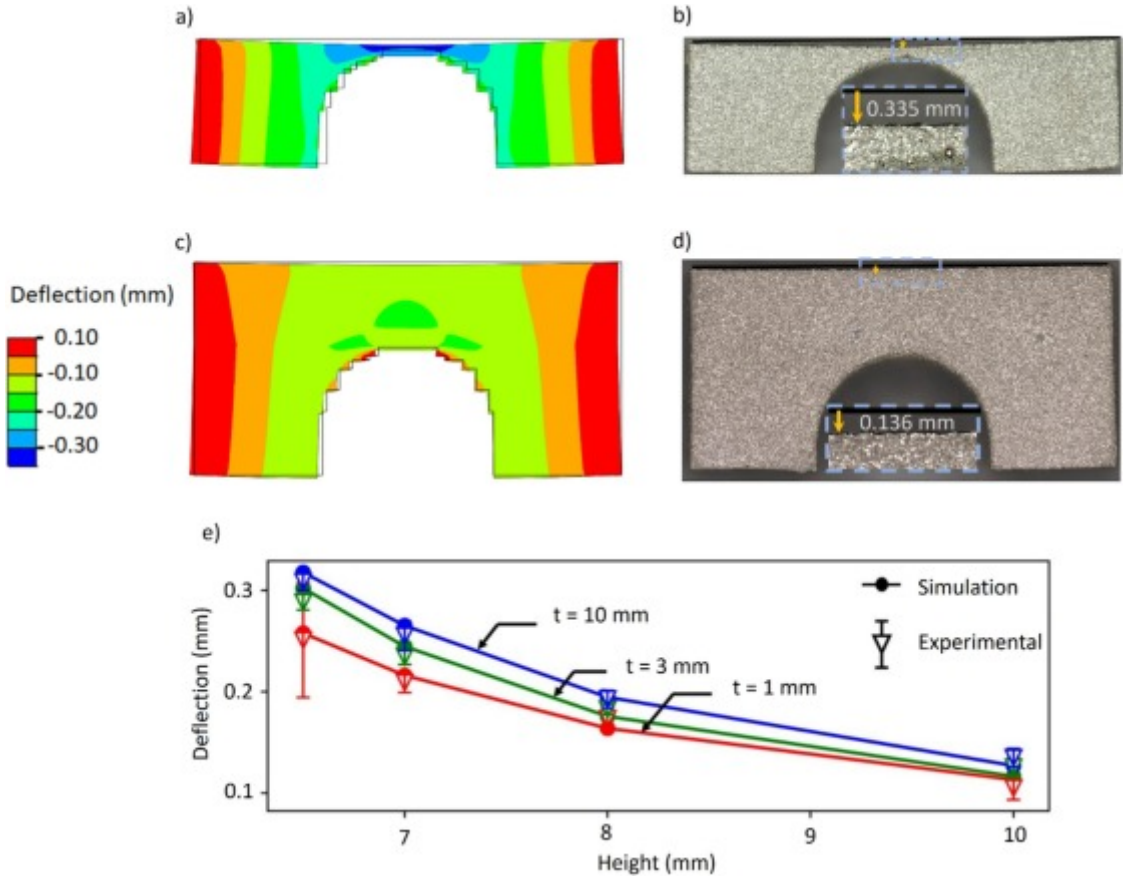
1. Download: Download high-res image (480KB)
2. Download: Download full-size image

Fig. 7. (a-d) Stress contours of σ_{VM}, σ_{11}, σ_{22}, and σ_{33} for the bridge specimen with the height of 10 mm and thickness of 3 mm and (e-g) Stress profiles of σ_{11}, σ_{22}, and σ_{33} along the height for the bridge specimen with the height of 10 mm and thickness of 1 and 10 mm.

To further investigate the geometric effect on stress profiles, Fig. 7e - Fig. 7g compare the stress profiles of bridge specimens with thicknesses of 1 mm and 10 mm, both having an identical height of 10 mm. We plotted the stress profiles of σ_{11}, σ_{22}, and σ_{33} from the substrate through the bridge. The stress extraction was carried out at one of the bridge's anchors. According to Fig. 7e - Fig. 7g, although the stress profiles of both samples are similar, we noticed a difference in the part-substrate interface. For example, the compressive stress of σ_{11} at the interface changes from 260 MPa to 420 MPa, nearly twice as large, when the thickness increases from 1 mm to 10 mm. These results indicate that the specimen with a larger volume leads to a greater amount of residual stress retained by the substrate. Therefore, when the parts are removed from the substrate, specimens with larger stresses in the substrate would result in greater stress relaxation.

Subsequently, the substrate removal was performed and simulated similarly. We performed a two-step mechanical simulation. In the first step, we only considered the layer-by-layer build-up approach, where the samples were assumed to be fully attached to the substrate. Subsequently, after the build process was completed, we removed the substrate to capture the influence of stress relaxation and part deflection. Fig. 8a to Fig. 8b shows the deformation patterns from both simulation and experiment for the sample with a height and thickness of 6.5 and 10 mm, respectively. The black solid

line in Fig. 8a denotes the original model without any deformation. Similarly, simulated and experimental samples were also shown for the sample with a height and thickness of 10 and 1 mm, as seen in Fig. 8c to Fig. 8d. Overall, it was observed that deformation patterns were agreeable for both numerical and experimental results. After the substrate removal, the bridge is deflected, with a concave curve seen at the top surface. However, we also noticed that the curvature magnitude changes relative to geometric parameters. The sample with greater height shows smaller deflection when compared to Fig. 8a and Fig. 8b with Fig. 8c and Fig. 8d. Therefore, a comprehensive parametric study was performed for the bridge samples with heights between 6.5, 7, 8, and 10 mm, as well as three different thicknesses between 1, 3, and 10 mm. In total, 12 different bridge samples were examined. The computational time was determined for each case. We found that the required time increases with higher and thicker specimens. The computational time was found to be between 0.75 and 9.45 h, in which more details of required resource was shown in the Appendix. Predicted and measured deflections of all samples are shown in Fig. 8e. According to Fig. 8e, greater deflection was observed for thicker and shorter specimens. As mentioned previously, thicker specimens led to larger residual stress reserved in the substrate. Therefore, greater deflection was seen as a result of stress redistribution. On the other hand, specimens with greater heights led to enhanced structural rigidity, which, in turn, limits the deflection of the bridge upon the relaxation process. For this reason, the effect of thickness was more apparent for shorter samples. For example, at a height of 6.5 mm, the deflection increases from 0.25 to 0.3 mm when the thickness changes from 1 to 10 mm, which accounts for approximately a 20 % change. However, at a height of 10 mm, the change in deflection was only around 10 % under the same change in thickness. Additionally, Fig. 8e also demonstrates the capability of the modified inherent strain method in capturing the geometric effect on residual stress and deflection. A similar qualitative and quantitative trend between experiment and numerical prediction is observed. This finding extends the exploration of the modified inherent strain method for samples with large geometric variations.

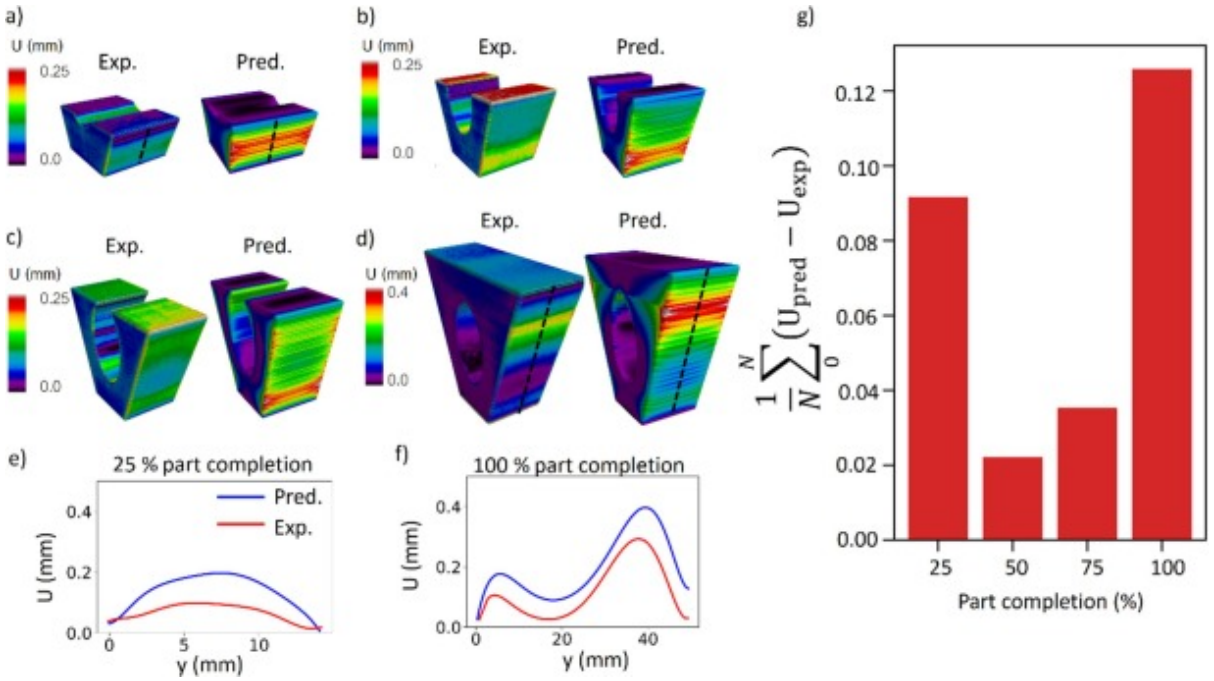


1. Download: Download high-res image (370KB)
2. Download: Download full-size image

Fig. 8. Numerical and experimental contours of relaxed distortion of the bridge sample with height, thickness of 6.5 mm, 10 mm (a-b) and 10 mm, 1 mm (c-d). Predicted and measured deflection of the bridge with heights between 6.5, 7, 8, and 10 mm as well as three different thicknesses between 1, 3, and 10 mm.

4.3. Examination of as-built distortion in wedge specimens

In addition to the relaxed distortion, as-built distortion has been examined. The wedge samples with thicknesses varied from 1 to 20 mm were printed and subjected to 3D scanning. Distortion contours were compared with the original CAD geometry, in which the deviation between both results was defined as the as-built distortion. The modified inherent strain method was carried out in parallel to predict as-built distortion. Fig. 9a to Fig. 9d show measured and predicted distortion contours for the wedge with 20 mm thickness. According to Fig. 9a to Fig. 9d, instead of considering a fully completed part, we designed the specimens to be at different build stages from 25, 50, 75, to 100 % completion. A distortion comparison at different build stages would allow us to comprehensively evaluate the capacity and limitations of the numerical framework.



1. Download: Download high-res image (303KB)
2. Download: Download full-size image

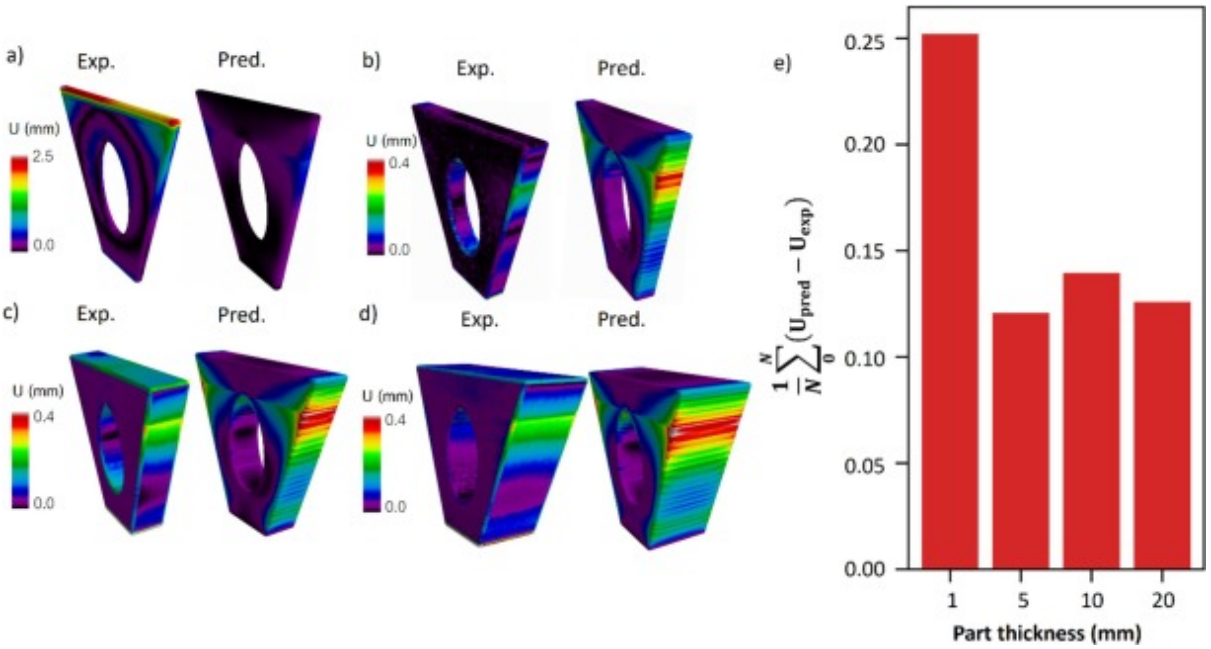
Fig. 9. Measured and predicted distortion contours for the wedge with 20 mm thickness at a) 25 %, b) 50 %, c) 75 %, and d) 100 % build stages, distortion profiles along the side edge of the wedge at e) 25 % and f) 100 % build completion, and g) average difference between the distortion profiles from measurement and prediction at different build stages.

By considering the distortion of inclined surfaces from Fig. 9a to Fig. 9c, we found that distortion was observed in the region slightly above the substrate. Additionally, considering Fig. 9d, when the build is completed, we noticed a large distortion near the overhang region of the wedge, which shows that the change in the cross-section of the specimens could affect the distortion profiles. The numerical framework was able to qualitatively capture the distortion of progressive builds from 25 % to 100 %, demonstrating the capability of the inherent strain framework in estimating complex as-built distortion.

In Fig. 9e and Fig. 9f, we considered more closely the deviation between numerical and experimental results at a quarter of the build and when the build is completed. The distortion profiles were plotted along the centerline of the inclined surface, as denoted by the black dashed lines in Fig. 9a and Fig. 9d. Fig. 9e shows the distortion profile at 25 % build. Both the numerical model and the experiment exhibit a similar qualitative trend with the maximum distortion seen at a y-distance of 7.5 mm. Additionally, the distortion exhibits a concave shape, with minimal distortion at both ends of the specimens. However, the distortion magnitude was higher in the numerical results, with the maximum difference being approximately 0.1 mm. The distortion profile at 100 % build is shown in Fig. 9f. A bimodal pattern was observed, with the maximum distortion occurring at y-distances of 5 and 40 mm. The second peak at 40 mm shows much higher distortion compared to the peak at 5 mm. Interestingly, both numerical and experimental results exhibit a similar trend, but the distortion magnitude differed by around 0.1 mm at both peaks. In addition, we hypothesized the reasons for the bimodal distortion profiles observed in Fig. 9f as follows. Firstly, the distortion at the substrate is mostly zero due to mechanical constraints at the part-substrate interface. Then, the distortion increases continuously

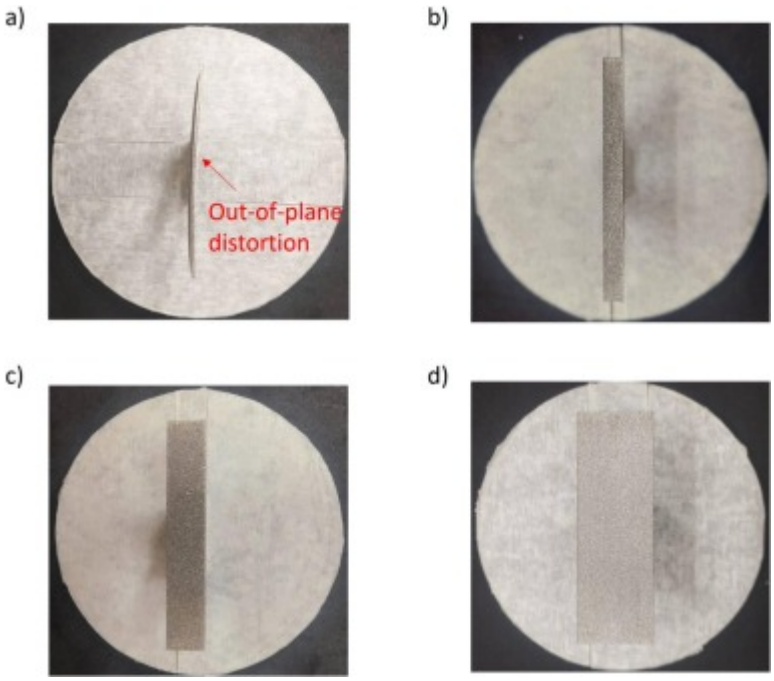
when the surface away from the part-substrate interface is considered, mainly due to smaller mechanical restrictions. However, when we approach the ellipsoid region, the distortion is reduced. This is mainly due to smaller stress contraction since the cross-section area of the ellipsoidal region is smaller than that of the bulk part. Lastly, when the overhang region at the end of the ellipsoidal hole is considered, the second peak in the bimodal pattern is observed. This is mainly driven by the strong contraction force from the bulk region at the top of the ellipsoid, which induces noticeable distortion. Followingly, Fig. 9g illustrates the average difference between predicted and measured results, which varied between 0.02 and 0.12 mm.

Additionally, Fig. 10a to Fig. 10d explored the distortion profiles of the wedge with thicknesses varied from 1, 5, 10, and 20 mm, respectively. To complete the simulation for all four wedges, the computational time was 14, 20, 25, and 37 h, respectively. Additionally, although Fig. 10b to Fig. 10d showed that numerical prediction could capture the distortion profiles of the wedge at the thicknesses of 5, 10, and 20 mm, significant deviation was seen for the thin wedge at 1 mm. Fig. 10e determined the deviation between experimental and numerical results. For the wedges of 5, 10, and 20 mm thickness, the average difference was around 0.12 and 0.14 mm. However, if the wedge of 1 mm thickness is considered, the deviation between measured and predicted results becomes significantly higher. To explore further, Fig. 11 displayed the printed wedges with thicknesses of 1, 5, 10, and 20 mm, respectively. Noticeably, the out-of-plane distortion was observed at the thin wedge. Nonetheless, we did not observe the out-of-plane behavior at thicker wedges as well as in numerical simulations.



1. Download: Download high-res image (245KB)
2. Download: Download full-size image

Fig. 10. Measured and predicted distortion contours for the wedge with a) 1 mm, b) 5 mm, c) 10 mm, d) 20 mm thickness, and e) average difference between distortion profiles from measurement and prediction for the wedges with different thicknesses.



1. Download: Download high-res image (201KB)
2. Download: Download full-size image

Fig. 11. Experimental distortion profiles of a) 1 mm, b) 5 mm, c) 10 mm, and d) 20 mm from the top views.

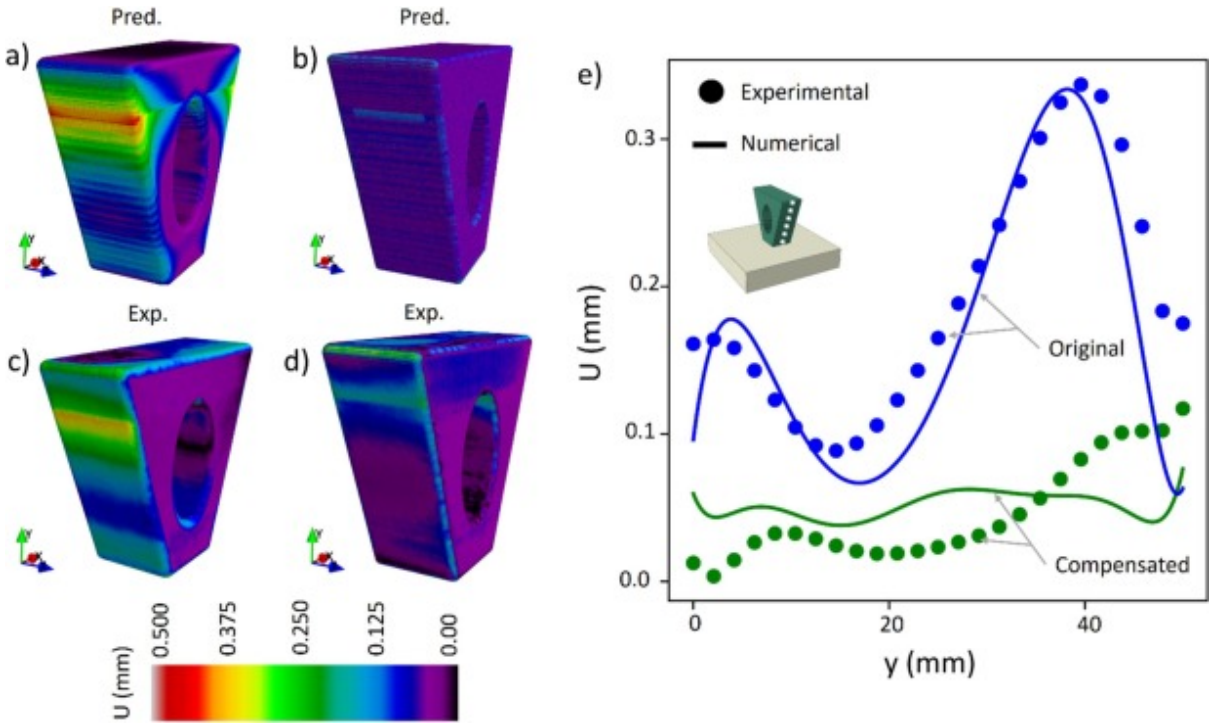
According to Fig. 10 and Fig. 11, if we examined the difference between measured and predicted distortion, we could divide the reasons for two geometry ranges, which are thick parts and thin parts. For thick parts, we refer to specimens with thicknesses between 5 and 20 mm, and for thin parts, we refer to a specimen with a thickness of 1 mm. For the thick parts, we found that the simulation provided reasonably accurate distortion with an average deviation of less than 0.15 mm, as shown in Fig. 10d. Thus, the difference between simulation and experiment may be due to undersizing and oversizing of specimens as described in Sombatmai et al. [48], where the printed part can appear smaller or larger than the CAD model. For the thin parts, we found that the difference in distortion increased to 0.25 mm, where the out-of-plane distortion contributed significantly to the difference. As a result, there exist physical phenomena in the residual stress formation in the AM process, which are not well-captured by the modified inherent strain approach.

In this regard, numerical results from Section 4.1 imply that the material activation patterns in the modified inherent strain method do not largely contribute to the change in distortion observed in thin samples. Other possible scenarios could be the effect of recoater-induced distortions as presented by Lu et al. [51], as well as buckling behaviors as reported by Vastola et al. [52]. Such effects on out-of-plane distortion in thin specimens could be a topic of future study.

4.4. Evaluation of geometrical compensation

Although the out-of-plane distortion in thin specimens requires further investigation, we evaluate the distortion compensation in bulk specimens. A primary advantage of a high-fidelity prediction framework is its ability to perform geometrical compensation for as-built distortion. To analyze the effectiveness of the current framework, we tested geometrical compensation with a wedge of 20 mm thickness both numerically and experimentally. For the numerical testing, Fig. 12a shows the predicted distortion of the wedge based on the original CAD model. Based on these distortion results,

we created the compensated CAD model using the approach described in Section 3.3. Subsequently, we repeated the part-scale calculation with the compensated geometry, and the distortion results were compared with the original CAD model, as shown in Fig. 12b. Overall, it was noticed that the distortion reduced significantly once the geometrical compensation strategy was adopted.



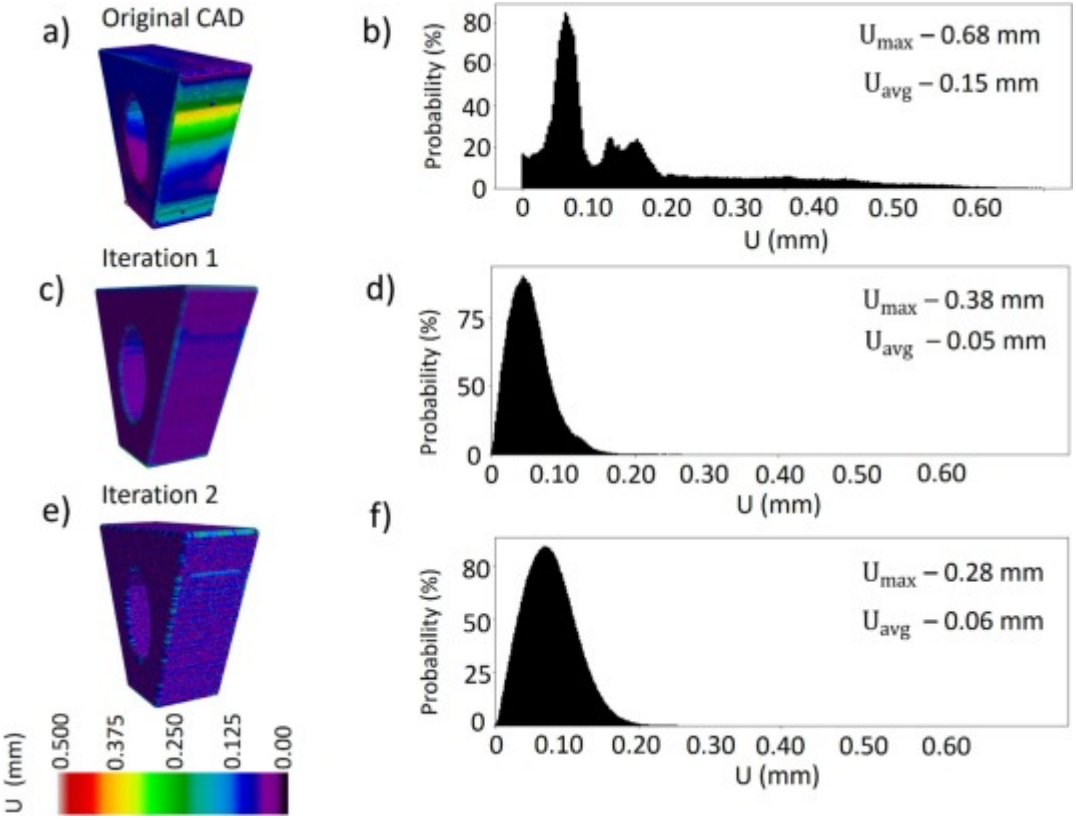
1. Download: Download high-res image (306KB)
2. Download: Download full-size image

Fig. 12. a) Predicted distortion of original CAD model, b) predicted distortion of compensated model, c) measured distortion of printed CAD model, d) measured distortion of printed compensated model, and e) comparison of predicted and measured distortion of original and compensated models at the inclined surfaces.

Following this, experimental testing of the compensation strategy was carried out, as shown in Fig. 12c and Fig. 12d for the original and compensated models, respectively. Evidently, the experimental results agree well with the numerical predictions, indicating the effectiveness of geometrical compensation in minimizing as-built distortion. Additionally, we analyzed the distortion profiles of the inclined surfaces, as shown in Fig. 12e. Overall, both numerical predictions and experimental results show reasonable agreement of distortion profiles. Additionally, we noticed that geometrical compensation could reduce both maximum and average distortion. The maximum distortion reduced from 0.33 to 0.13 mm, and the average distortion reduced from 0.15 to 0.06 mm owing to the geometrical compensation strategy. Overall, the modified inherent strain framework was shown to resolve as-built distortion with satisfactory outcomes.

It should be noted that the previous results from Fig. 12 were performed with a single geometrical compensation. In fact, we could repeat the compensation multiple times based on the previously compensated geometry. However, as multiple compensations lead to substantial resource requirements, their benefits were evaluated, as shown in Fig. 13. Based on Fig. 13a to Fig. 13f, we performed geometrical compensation using two iterations. The as-built distortion of the original geometry is shown in Fig. 13a to Fig. 13b, as-built distortion of the first iteration in Fig. 13c to Fig. 13d,

and as-built distortion of the second iteration in Fig. 13e to Fig. 13f. Of note, the compensation of the second iteration was based on the distorted geometry from the first one. Overall, the second iteration did not result in a significant improvement in geometrical correction. While the first iteration reduced the average distortion from 0.15 to 0.05 mm, the second iteration resulted in a similar average distortion as the first one. This finding implies that to perform geometrical compensation, a single iteration would be sufficient.



1. Download: Download high-res image (259KB)
2. Download: Download full-size image

Fig. 13. Distortion contours and deviation profiles of (a-b) original CAD geometry, (c-d) compensated CAD geometry of the first iteration, and (e-f) compensated CAD geometry of the second iteration.

4.5. Outlook for future work

The present work has evaluated the modified inherent strain method in capturing relaxed deflection and as-built distortion of additively manufactured specimens with varied configuration. The results showed that the modified inherent strain method can capture both deflection and as-built distortion with reasonable accuracy. Nevertheless, we found that many aspects could be explored further in future studies, and they are described herein. Firstly, although we did not observe much difference in predicted stress and distortion between layer-by-layer and track-by-track depositions, the effects of the track-by-track scheme could be more pronounced with more complex geometries. This issue could be addressed more thoroughly in future work. However, it is evident that applying track-by-track deposition significantly increases computational costs. These resources continue to increase with greater thickness and height. Therefore, the efficient implementation of track-by-track deposition at the part-scale level may require the development of a multi-scale strategy, which could minimize resource usage while maintaining accurate predictions. Secondly, while the present results showed that multiple compensations demonstrate a slight improvement in geometrical correction, this

observation specifically applies to the geometry examined in the present work. Under different process conditions and more complex geometrical configurations, the advantages of multiple iterations may become more noticeable. In addition, the computational strategy that could capture out-of-plane distortion should be assessed. The integration of the buckling phenomenon, as explored previously by Vastola et al. [52], could be considered in future work. Lastly, to further reduce the computational cost of distortion prediction, the use of explicit FEM and GPU acceleration, as demonstrated previously by Huang et al. [53] and Liao et al. [54], could be considered. Alternatively, a data-driven method could also be applied, as shown in the study of Dong et al. [55]. Finite Element (FE) simulation and experimental results could be used together as input for training a machine learning model. With a data-driven approach, one may explore the distortion response under varied process conditions and geometrical variations with better comprehension.

5. Conclusions

The present work explores distortion prediction and geometry compensation of additively manufactured Ti-6Al-4V using the modified inherent strain method. In contrast to previous works in this domain, we considered both relaxed distortion from substrate removal as well as as-built distortion. The specimens considered in the present work contain geometrical variations such as height and thickness. The overall aim is to comprehensively examine the benefits and limitations of the modified inherent strain approach in capturing distortion in different build scenarios. In addition to examining distortion, we explore the influence of material deposition in the modified inherent strain approach and evaluate the effectiveness of the geometrical compensation method in minimizing as-built distortion. Based on the results of the present study, the following conclusions can be drawn:

- 1.

The effect of track-by-track and layer-by-layer deposition on distortion was studied. From both deposition patterns, we did not observe a significant change in predicted distortion. Under conditions explored in the present work, the effect of deposition patterns results in different predicted distortions of less than 0.008 mm.

- 2.

We built bridge samples with heights ranging from 6.5 to 10 mm and thicknesses from 1 to 10 mm. The deflection after substrate removal increases with shorter height and greater thickness and could vary between 0.1 and 0.3 mm. The deflection results from numerical simulations match reasonably well with experiments, demonstrating the capability of the numerical approach in capturing stress states of samples with varied geometrical features.

- 3.

The wedges with ellipsoidal holes with thicknesses of 1, 5, 10, and 20 mm were built to capture as-built distortion. We found that the numerical model could capture the as-built distortion of samples with thicknesses of 5, 10, and 20 mm, where the average deviation between numerical and experimental was approximately 0.125 mm.

- 4.

Nonetheless, out-of-plane distortion was observed in the thin wedge of 1 mm, and the numerical model based on the modified inherent strain method was unable to capture such behaviors. Other influencing factors such as recoater blade and buckling were suggested and could potentially be explored in future studies.

- 5.

Based on the predicted distortion of the original geometry, compensated geometry was generated to

alleviate as-built distortion. Based on the compensation framework, the maximum distortion reduced from 0.68 to 0.28 mm, and the average distortion reduced from 0.15 to 0.05 mm, demonstrating the effectiveness of the proposed strategy.

- 6.

We explored further the influence of multiple geometrical compensations in minimizing as-built distortion. However, we found that the distortion results between the first and second iterations differed insignificantly. Both iterations exhibit an average distortion of approximately 0.15 mm. Thus, based on the conditions explored in the present work, a single compensation was deemed sufficient for distortion alleviation.

CRediT authorship contribution statement

Refak Makeen: Writing – review & editing, Writing – original draft, Visualization, Validation, Software, Resources, Project administration, Methodology, Investigation, Formal analysis, Data curation. **Kartikey Joshi:** Writing – review & editing, Writing – original draft, Visualization, Validation, Software, Methodology, Formal analysis. **Mark H. Jhon:** Writing – review & editing, Writing – original draft, Supervision, Funding acquisition, Formal analysis, Conceptualization. **Patcharapit Promoppatum:** Writing – review & editing, Writing – original draft, Visualization, Supervision, Resources, Project administration, Methodology, Funding acquisition, Conceptualization.

Declaration of generative AI and AI-assisted technologies in the writing process

During the preparation of this work, the authors used *ChatGPT* to improve readability. After using this tool, the authors reviewed and edited the content as needed and take full responsibility for the content of the publication.

Declaration of competing interest

The authors declare that they have no known competing financial interests or personal relationships that could have appeared to influence the work reported in this paper.

Acknowledgements

RM acknowledges KMUTT International Scholarship Program (KISP) and Petch Pra Jom Klao Master's Degree Research Scholarship from King Mongkut's University of Technology Thonburi. PP acknowledges the financial support from National Research Council of Thailand (Grant number N42A660524) and Thailand Science Research and Innovation (TSRI) under Fundamental Fund 2024 (Project: Advanced Materials and Manufacturing for Applications in new S-curve industries). MJ and KJ gratefully acknowledge funding from A*STAR, Singapore via the Structural Metals and Alloys Programme (No. A18B1b0061).

Appendix A.

Table 3 summarized the computational time for wedge under different geometrical variations and deposition patterns. Of note, for the wedge specimens, the track-by-track deposition was only performed for the part with thicknesses of 1 and 20 mm. In addition, Table 4 shows the required computational time for bridge-like specimens under varied heights and thicknesses. It should be noted that the simulation was run on the same workstation for all cases.

Table 3. Computational time for wedge under different thicknesses and different deposition patterns.

Wedge thickness (mm)	Computational time with layer-by-layer deposition (hours)	Computational time with track-by-track deposition (hours)
1	14	56
5	20	–

Wedge thickness (mm)	Computational time with layer-by-layer deposition (hours)	Computational time with track-by-track deposition (hours)
10	25	–
20	37	1650

Table 4. Computational time for bridge structures under different thicknesses and heights.

Empty Cell		Thickness		
		1 mm	3 mm	10 mm
Height	**6.5 mm**	0.79 h	0.83 h	0.75 h
	7 mm	0.83 h	1.36 h	3.44 h
	8 mm	0.94 h	1.65 h	5.98 h
	10 mm	1.19 h	2.19 h	9.45 h

Data availability statement

Data will be made available on request.

References

1. [1]

W.E. Frazier

Metal additive manufacturing: a review

J Mater Eng Perform, 23 (6) (2014), pp. 1917-1928, 10.1007/s11665-014-0958-z

View in ScopusGoogle Scholar

2. [2]

Petrick, I. J., and Simpson, T. W., 2013, “3D Printing Disrupts Manufacturing: How Economies of One Create New Rules of Competition,” null, 56(6), pp. 12–16. doi:https://doi.org/10.5437/08956308X5606193.

Google Scholar

3. [3]

K.V. Wong, A. Hernandez

A review of additive manufacturing

International scholarly research notices, 2012 (2012)

Google Scholar

4. [4]

M.F. Zaeh, G. Branner

Investigations on residual stresses and deformations in selective laser melting

Prod Eng, 4 (1) (2010), pp. 35-45, 10.1007/s11740-009-0192-y

View in ScopusGoogle Scholar

5. [5]

P. Mercelis, J.-P. Kruth

Residual stresses in selective laser sintering and selective laser melting

(2006)

[Rapid prototyping journal]

Google Scholar

6. [6]
M.S. Moyle, N. Haghdadi, V. Luzin, F. Salvemini, X.Z. Liao, S.P. Ringer, *et al.*
Correlation of microstructure, mechanical properties, and residual stress of 17-4 PH stainless steel fabricated by laser powder bed fusion
J Mater Sci Technol, 198 (2024), pp. 83-97, 10.1016/j.jmst.2024.01.080
View PDFView articleView in ScopusGoogle Scholar
7. [7]
N.C. Levkulich, S.L. Semiatin, J.E. Gockel, J.R. Middendorf, A.T. DeWald, N.W. Klingbeil
The effect of process parameters on residual stress evolution and distortion in the laser powder bed fusion of Ti-6Al-4V
Addit Manuf, 28 (2019), pp. 475-484
View PDFView articleView in ScopusGoogle Scholar
8. [8]
I. Serrano-Munoz, T. Fritsch, T. Mishurova, A. Trofimov, D. Apel, A. Ulbricht, *et al.*
On the interplay of microstructure and residual stress in LPBF IN718
J Mater Sci, 56 (2021), pp. 5845-5867
CrossrefView in ScopusGoogle Scholar
9. [9]
S. Chen, H. Gao, Y. Zhang, Q. Wu, Z. Gao, X. Zhou
Review on residual stresses in metal additive manufacturing: formation mechanisms, parameter dependencies, prediction and control approaches
J Mater Res Technol, 17 (2022), pp. 2950-2974, 10.1016/j.jmrt.2022.02.054
View PDFView articleGoogle Scholar
10. [10]
Hajnys, J., Pagáč, M., Měsíček, J., Petru, J., and Król, M., 2020, “Influence of Scanning Strategy Parameters on Residual Stress in the SLM Process According to the Bridge Curvature Method for AISI 316L Stainless Steel,” Materials, **13**(7), p. 1659.
Google Scholar
11. [11]
S. Goel, M. Neikter, J. Capek, E. Polatidis, M.H. Colliander, S. Joshi, *et al.*
Residual stress determination by neutron diffraction in powder bed fusion-built alloy 718: influence of process parameters and post-treatment
Mater Des, 195 (2020), p. 109045, 10.1016/j.matdes.2020.109045
View PDFView articleView in ScopusGoogle Scholar
12. [12]
P. Promoppatum, S.-C. Yao
Influence of scanning length and energy input on residual stress reduction in metal additive manufacturing: numerical and experimental studies
J Manuf Process, 49 (2020), pp. 247-259, 10.1016/j.jmapro.2019.11.020
View PDFView articleView in ScopusGoogle Scholar
13. [13]
R.J. Williams, F. Vecchiato, J. Kelleher, M.R. Wenman, P.A. Hooper, C.M. Davies
Effects of heat treatment on residual stresses in the laser powder bed fusion of 316L stainless steel: finite element predictions and neutron diffraction measurements

J Manuf Process, 57 (2020), pp. 641-653, 10.1016/j.jmapro.2020.07.023
View PDFView articleView in ScopusGoogle Scholar
14. [14]
A. Pathania, A.K. Subramaniyan, B. Nagesha
Influence of post-heat treatments on microstructural and mechanical properties of LPBF-processed Ti6Al4V alloy
Progress in Additive Manufacturing, 7 (6) (2022), pp. 1323-1343
CrossrefView in ScopusGoogle Scholar
15. [15]
Barros, R., Silva, F. J., Gouveia, R. M., Saboori, A., Marchese, G., Biamino, S., Salmi, A., and Atzeni, E., 2019, "Laser Powder Bed Fusion of Inconel 718: Residual Stress Analysis before and after Heat Treatment," Metals, **9**(12), p. 1290.
Google Scholar
16. [16]
X. Chen, X. Xie, H. Wu, X. Ji, H. Shen, M. Xue, *et al.*
In-situ control of residual stress and its distribution in a titanium alloy additively manufactured by laser powder bed fusion
Mater Charact, 201 (2023), p. 112953, 10.1016/j.matchar.2023.112953
View PDFView articleView in ScopusGoogle Scholar
17. [17]
E.R. Denlinger, M. Gouge, J. Irwin, P. Michaleris
Thermomechanical model development and in situ experimental validation of the laser powder-bed fusion process
Addit Manuf, 16 (2017), pp. 73-80
View PDFView articleView in ScopusGoogle Scholar
18. [18]
R. Ganeriwala, M. Strantza, W. King, B. Clausen, T. Phan, L. Levine, *et al.*
Evaluation of a thermomechanical model for prediction of residual stress during laser powder bed fusion of Ti-6Al-4V
Addit Manuf, 27 (2019), pp. 489-502
View PDFView articleView in ScopusGoogle Scholar
19. [19]
H. Murakawa, D. Deng, N. Ma, J. Wang
Applications of inherent strain and Interface element to simulation of welding deformation in thin plate structures
Comput Mater Sci, 51 (1) (2012), pp. 43-52
View PDFView articleView in ScopusGoogle Scholar
20. [20]
B. Yi, J. Wang
Mechanism clarification of mitigating welding induced buckling by transient thermal tensioning based on inherent strain theory
J Manuf Process, 68 (2021), pp. 1280-1294
View PDFView articleView in ScopusGoogle Scholar
21. [21]

H. Mohammadtaheri, R. Sedaghati, M. Molavi-Zarandi
Inherent strain approach to estimate residual stress and deformation in the laser powder bed fusion process for metal additive manufacturing—a state-of-the-art review
Int J Adv Manuf Technol, 122 (5–6) (2022), pp. 2187-2202
CrossrefView in ScopusGoogle Scholar

22. [22]
P. Promoppatum, V. Uthaisangsuk
Part scale estimation of residual stress development in laser powder bed fusion additive manufacturing of Inconel 718
Finite Elem Anal Des, 189 (2021), p. 103528
View PDFView articleView in ScopusGoogle Scholar

23. [23]
F. Bayerlein, F. Bodensteiner, C. Zeller, M. Hofmann, M.F. Zaeh
Transient development of residual stresses in laser beam melting–a neutron diffraction study
Addit Manuf, 24 (2018), pp. 587-594
View PDFView articleView in ScopusGoogle Scholar

24. [24]
C. Bayraktar, E. Demir
A thermomechanical finite element model and its comparison to inherent strain method for powder-bed fusion process
Addit Manuf, 54 (2022), p. 102708
View PDFView articleView in ScopusGoogle Scholar

25. [25]
N. Patil, R. Ganeriwala, J.M. Solberg, N.E. Hodge, R.M. Ferencz
Benchmark multi-layer simulations for residual stresses and deformation in small additively manufactured metal parts
Addit Manuf, 45 (2021), p. 102015
View PDFView articleView in ScopusGoogle Scholar

26. [26]
M. Jimenez Abarca, R. Darabi, J.C. de Sa, M. Parente, A. Reis
Multi-scale modeling for prediction of residual stress and distortion in Ti–6Al–4V semi-circular thin-walled parts additively manufactured by laser powder bed fusion (LPBF)
Thin-Walled Struct, 182 (2023), p. 110151, 10.1016/j.tws.2022.110151
View PDFView articleView in ScopusGoogle Scholar

27. [27]
Y. Chen, Y. Liu, H. Chen, Y. Wu, J. Chen, J. Xiong, *et al.*
Multi-scale residual stress prediction for selective laser melting of high strength steel considering solid-state phase transformation
Opt Laser Technol, 146 (2022), p. 107578
View PDFView articleView in ScopusGoogle Scholar

28. [28]
Q. Chen, X. Liang, D. Hayduke, J. Liu, L. Cheng, J. Oskin, *et al.*
An inherent strain based multiscale modeling framework for simulating part-scale residual deformation for direct metal laser sintering

Addit Manuf, 28 (2019), pp. 406-418
View PDFView articleView in ScopusGoogle Scholar
29. [29]
X. Liang, L. Cheng, Q. Chen, Q. Yang, To, A. C
A modified method for estimating inherent strains from detailed process simulation for fast residual distortion prediction of single-walled structures fabricated by directed energy deposition
Addit Manuf, 23 (2018), pp. 471-486
View PDFView articleView in ScopusGoogle Scholar
30. [30]
S. Afazov, E. Semerdzhieva, D. Scrimieri, A. Serjouei, B. Kairoshev, F. Derguti
An improved distortion compensation approach for additive manufacturing using optically scanned data
Virtual Phys Prototyp, 16 (1) (2021), pp. 1-13, 10.1080/17452759.2021.1881702
View in ScopusGoogle Scholar
31. [31]
S. Afazov, W.A.D. Denmark, B. Lazaro Toralles, A. Holloway, A. Yaghi
Distortion prediction and compensation in selective laser melting
Addit Manuf, 17 (2017), pp. 15-22, 10.1016/j.addma.2017.07.005
View PDFView articleView in ScopusGoogle Scholar
32. [32]
I. Setien, M. Chiumenti, S. van der Veen, M. San Sebastian, F. Garciandía, A. Echeverría
Empirical methodology to determine inherent strains in additive manufacturing
Comput Math Appl, 78 (7) (2019), pp. 2282-2295, 10.1016/j.camwa.2018.05.015
View PDFView articleView in ScopusGoogle Scholar
33. [33]
S. Afazov, H. Rahman, A. Serjouei
Investigation of the right first-time distortion compensation approach in laser powder bed fusion of a thin manifold structure made of Inconel 718
J Manuf Process, 69 (2021), pp. 621-629, 10.1016/j.jmapro.2021.08.016
View PDFView articleView in ScopusGoogle Scholar
34. [34]
Sedlacek, F., Kalina, T., and Stepanek, M., 2023, “Optimization of Components with Topology Optimization for Direct Additive Manufacturing by DLMS,” Materials, **16**(15), p. 5422.
Google Scholar
35. [35]
Kruth, J.-P., Deckers, J., Yasa, E., and Wauthlé, R., 2012, “Assessing and Comparing Influencing Factors of Residual Stresses in Selective Laser Melting Using a Novel Analysis Method,” Proceedings of the institution of mechanical engineers, Part B: Journal of Engineering Manufacture, 226(6), pp. 980–991.
Google Scholar
36. [36]
S. Le Roux, M. Salem, A. Hor
Improvement of the bridge curvature method to assess residual stresses in selective laser melting
Addit Manuf, 22 (2018), pp. 320-329

View PDFView articleView in ScopusGoogle Scholar

37. [37]

Ma, Q.-P., Mesicek, J., Fojtik, F., Hajnys, J., Krpec, P., Pagac, M., and Petru, J., 2022, “Residual Stress Build-Up in Aluminum Parts Fabricated with SLM Technology Using the Bridge Curvature Method,” Materials, **15**(17), p. 6057.

Google Scholar

38. [38]

Lestandi, L., Wong, J., Dong, G., Kuehsamy, S., Mikula, J., Vastola, G., Kizhakkinan, U., Ford, C., Rosen, D., and Dao, M., 2023, “Data-Driven Surrogate Modelling of Residual Stresses in Laser Powder-Bed Fusion,” International Journal of Computer Integrated Manufacturing, pp. 1–23.

Google Scholar

39. [39]

P. Promoppatum, B. Chayasombat, A.N. Soe, A. Sombatmai, Y. Sato, T. Suga, *et al.*

In-situ modification of thermal, microstructural, and mechanical responses by altering scan lengths in laser powder bed fusion additive manufacturing of Ti-6Al-4V

Opt Laser Technol, 164 (2023), p. 109525

View PDFView articleView in ScopusGoogle Scholar

40. [40]

R. Williams, M. Bilton, N. Harrison, P. Fox

The impact of oxidised powder particles on the microstructure and mechanical properties of Ti-6Al-4V processed by laser powder bed fusion

Addit Manuf, 46 (2021), p. 102181

View PDFView articleView in ScopusGoogle Scholar

41. [41]

A. Issariyapat, S. Kariya, K. Shitara, J. Umeda, K. Kondoh

Solute-induced near-isotropic performance of laser powder bed fusion manufactured pure titanium

Addit Manuf, 56 (2022), p. 102907

View PDFView articleView in ScopusGoogle Scholar

42. [42]

A. Bârsan, S.-G. Racz, R. Breaz, M. Crenganiş

Evaluation of the dimensional accuracy through 3D optical scanning in incremental sheet forming

Proceedings, Materials Today (2023)

Google Scholar

43. [43]

G. Vastola, G. Zhang, Q. Pei, Y.-W. Zhang

Controlling of residual stress in additive manufacturing of Ti6Al4V by finite element modeling

Addit Manuf, 12 (2016), pp. 231-239

View PDFView articleView in ScopusGoogle Scholar

44. [44]

P. Bian, J. Shi, Y. Liu, Y. Xie

Influence of laser power and scanning strategy on residual stress distribution in additively manufactured 316L steel

Opt Laser Technol, 132 (2020), p. 106477

View PDFView articleView in ScopusGoogle Scholar

45. [45]
Z. Xiao, C. Chen, H. Zhu, Z. Hu, B. Nagarajan, L. Guo, *et al.*
Study of residual stress in selective laser melting of Ti6Al4V
Materials & Design, p, 108846 (2020)
Google Scholar
46. [46]
W. Dong, X. Liang, Q. Chen, S. Hinnebusch, Z. Zhou, To, A. C
A new procedure for implementing the modified inherent strain method with improved accuracy in predicting both residual stress and deformation for laser powder bed fusion
Addit Manuf, 47 (2021), p. 102345
View PDFView articleView in ScopusGoogle Scholar
47. [47]
U.P. Singh, S. Swaminathan, G. Phanikumar
Thermo-mechanical approach to study the residual stress evolution in part-scale component during laser additive manufacturing of alloy 718
Mater Des, 222 (2022), p. 111048
View PDFView articleView in ScopusGoogle Scholar
48. [48]
A. Sombatmai, V. Uthaisangsuk, S. Wongwises, P. Promoppatum
Multiscale investigation of the influence of geometrical imperfections, porosity, and size-dependent features on mechanical behavior of additively manufactured Ti-6Al-4V lattice struts
Mater Des, 209 (2021), p. 109985, 10.1016/j.matdes.2021.109985
View PDFView articleView in ScopusGoogle Scholar
49. [49]
J. Wang, J. Zhang, G. Liu, L. Liang, G. Yang, A. Huang, *et al.*
Effects of scanning strategies on residual stress and deformation by high-power direct energy deposition: island size and laser jump strategy between islands
J Manuf Process, 75 (2022), pp. 23-40
View PDFView articleGoogle Scholar
50. [50]
K. Ren, Y. Chew, J. Fuh, Y. Zhang, G. Bi
Thermo-mechanical analyses for optimized path planning in laser aided additive manufacturing processes
Mater Des, 162 (2019), pp. 80-93
View PDFView articleView in ScopusGoogle Scholar
51. [51]
Lu, X., Chiumenti, M., Cervera, M., Slimani, M., and Gonzalez, I., 2023, “Recoater-Induced Distortions and Build Failures in Selective Laser Melting of Thin-Walled Ti6Al4V Parts,” Journal of Manufacturing and Materials Processing, **7**(2), p. 64.
Google Scholar
52. [52]
G. Vastola, W. Sin, C.-N. Sun, N. Sridhar
Design guidelines for suppressing distortion and buckling in metallic Thin-Wall structures built by powder-bed fusion additive manufacturing

Mater Des, 215 (2022), p. 110489
View PDFView articleView in ScopusGoogle Scholar
53. [53]
H. Huang, N. Ma, J. Chen, Z. Feng, H. Murakawa
Toward large-scale simulation of residual stress and distortion in wire and arc additive manufacturing
Addit Manuf, 34 (2020), p. 101248
View PDFView articleView in ScopusGoogle Scholar
54. [54]
S. Liao, A. Golgoon, M. Mozaffar, J. Cao
Efficient GPU-accelerated thermomechanical solver for residual stress prediction in additive manufacturing
Comput Mech, 71 (5) (2023), pp. 879-893
CrossrefView in ScopusGoogle Scholar
55. [55]
G. Dong, J.C. Wong, L. Lestandi, J. Mikula, G. Vastola, M.H. Jhon, *et al*.
A part-scale, feature-based surrogate model for residual stresses in the laser powder bed fusion process
J Mater Process Technol, 304 (2022), p. 117541
View PDFView articleView in ScopusGoogle Scholar